


SCIENTIFIC REPORTS



OPEN

Coral-like Co_3O_4 Decorated N-doped Carbon Particles as active Materials for Oxygen Reduction Reaction and Supercapacitor

Zhichao Lin & Xiuwen Qiao

Coral reef has a unique dendritic structure with large specific surface area, rich pore structure, so that it can be attached to a large number of zooxanthellae for gas exchange. Coral reef ecosystems are also known as underwater rainforests. Inspired by this biological structure, we designed and fabricated coral-like Co_3O_4 decorated N-doped carbon particles ($\text{Co}_3\text{O}_4/\text{N-CP}$). The obtained $\text{Co}_3\text{O}_4/\text{N-CP-900}$ catalyst shows efficient ORR electrocatalytic performances in an alkaline medium with a positive onset and half-wave potentials of 0.97 and 0.90V (vs. RHE), as well as a high diffusion-limited current density (5.50 mA cm^{-2}) comparable to that of a Pt/C catalyst (5.15 mA cm^{-2}). It also displays better stability and methanol tolerance than commercial Pt/C. In addition, the $\text{Co}_3\text{O}_4/\text{N-CP-900}$ electrode has a high specific capacitance of 316.2 F g^{-1} in 6 M KOH, as well as good rate capabilities and excellent cycle performance. These results are due to large surface area, narrow pore size distribution, high density electrochemical energy conversion and storage activity centers. This method presented here offers an effective path for the development of high performance multi-functional carbon-based materials for ORR and supercapacitor applications.

The development of new energy sources, such as fuel cells and supercapacitors, is the key to reduce the consumption of traditional energy. Therefore, numerous efforts have been devoted to the development of electrode catalysts for energy conversion and storage^{1,2}, in order to promote the commercialization of fuel cells and supercapacitors. Generally, platinum and its alloy catalysts are considered to be the most effective Oxygen Reduction Reaction (ORR) catalyst^{3,4}. However, they suffer from the expensive, limited resources, poor stability, which hinder its application in practice⁵. Due to the low cost and good stability of the heteroatom-doped carbon materials, they can be used as an ideal material for fuel cells^{6,7} and supercapacitors⁸. Recent studies have shown that the ORR activity of heteroatom-doped carbon materials is due to the redistribution of charge induced by doping around the heteroatom dopant, which reduces the ORR potential and changes the chemical adsorption of O_2 , effectively weakening O-O bonding⁹⁻¹². At the same time, heteroatom-doped carbon materials can be used as an electrode material for the supercapacitors, the introduction of heteroatoms in the carbon material can increase pseudocapacitance and improve the surface wettability, which is conducive to improving the performance of supercapacitors^{13,14}. Despite their considerable development, performance optimization is still needed to ensure that heteroatom-doped carbon materials can simultaneously satisfy requirements of ORR and supercapacitor.

In order to obtain efficient multi-functional materials for ORR and supercapacitors, the introduction of transition metal oxides (e.g., Co, Fe) into carbon materials doped with heteroatoms (e.g., N, S) may lead to electron modulation to provide an ideal electronic structure for relatively good electrocatalytic activity, which is considered to be an effective method^{15,16}. At the same time, we believe that the high specific surface area and narrow pore size distribution are also the key to determine the performance¹⁷⁻¹⁹. In nature, polyps adsorb iron, manganese and other elements during their formation, eventually forming a dendritic coral that is rich in pore structure. A kind of zooxanthella attached to the surface of the coral, converting the metabolic waste into O_2 and

Key Laboratory for Green Processing of Chemical Engineering of Xinjiang Bingtuan, State Key Laboratory Cultivation Base Jointly Constructed by Province and The Ministry, Key Laboratory of Materials-Oriented Chemical Engineering of Xinjiang Uygur Autonomous Region, College of Chemistry and Chemical Engineering, Shihezi University, Shihezi, 832000, China. Correspondence and requests for materials should be addressed to X.Q. (email: qxw_tea@shzu.edu.cn) or Z.L. (email: linzc@stu.shzu.edu.cn)

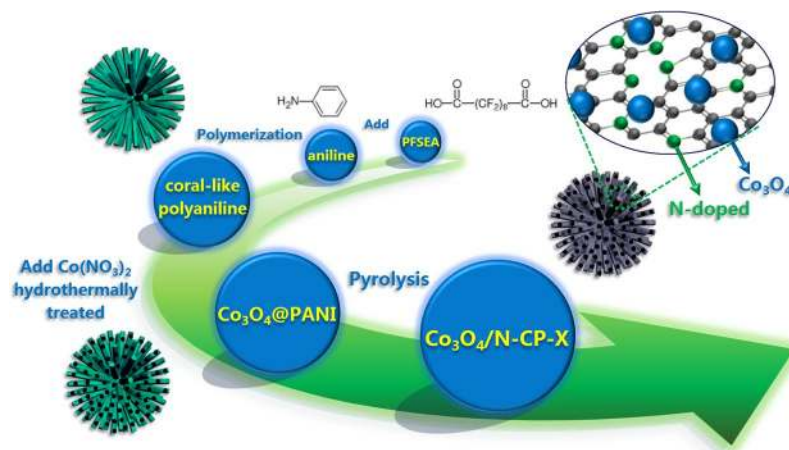


Figure 1. Scheme illustration of self-assembly with PANI and the derived Co₃O₄/N-CP-X.

carbohydrate by photosynthesis, and then returned to the polyyps (Fig. S1). Due to the high specific surface area, rich pore structure and gas exchange by the attachment of a large amount of zooxanthellae, coral reef ecosystems are also known as underwater rainforest^{20–22}. Inspired by this biological structure, we have tried to create a coral-like carbon structure that has a large specific surface area, abundant porous structure and incorporates the Co element on the surface. The structure acts like zooxanthellae to construct electrochemical energy conversion and store active center, which is conducive to the application of ORR and supercapacitors. This structure was similar to the symbiotic system of polyyps and zooxanthellae, expected to improve the electrochemical performance of carbon-based materials.

Herein, we have developed a simple, effective strategy for the preparation of the coral-like Co₃O₄ decorated N-doped carbon particles (Co₃O₄/N-CP-X) (X represents as temperature) for the first time. Co₃O₄/N-CP-X has been prepared through self-assembly of polyaniline (PANI) as the precursor, hydrothermal synthesis of Co₃O₄, and then pyrolysis, which displayed efficient catalytic activity for oxygen reduction and excellent capacitive properties in an alkaline solution (Fig. S2). In particular, the Co₃O₄/N-CP-900 acted as ORR electrocatalyst showing the positive onset and half-wave potentials (0.97 V and 0.90 V), basically compared to Pt/C catalyst (0.99 V and 0.89 V), and displayed high stability, good methanol tolerance in alkaline solution. Moreover, Co₃O₄/N-CP-900 can be used as electrode material for supercapacitor, with a high specific capacitance of 316.2 F g⁻¹ at a current density of 1 A g⁻¹, as well as long-term stability, good rate capabilities and excellent cycle performance. The improved electrochemical properties can be attributed to the high surface area, narrow pore size distribution and multi-element doping of the coral-like structure, which provides higher density of active sites, better obtaining electrolyte, greater ion storage space, faster electrolyte diffusion and movement for Co₃O₄/N-CP-X. This work provides an effective way to produce heteroatom-doped carbon materials for electrochemical energy conversion and storage.

Results and Discussion

Synthesis of Co₃O₄/N-CP-X. The typical synthetic steps of coral-like Co₃O₄/N-CP-X showed in Fig. 1. The coral-like polyaniline doped with perfluorosebacic acid (PANI/PFSEA) precursor was fabricated by chemical polymerization in the presence of aniline, PFSEA and Co(NO₃)₂·6H₂O acted as monomer, dopant and oxidant, respectively. Then coral-like Co₃O₄/N-CP-X particles (X represents pyrolysis temperature) were prepared by hydrothermal treatment of PANI/PFSEA and Co(NO₃)₂·6H₂O at 180 °C, thus leading to crystallization of Co₃O₄ and reduction of PANI to form the Co₃O₄/PANI hybrid²³, then followed by pyrolysis in tubular furnace at 800 °C, 900 °C, 1000 °C under the nitrogen atmosphere for 3.0 h with a heating rate of 5 °C/min, respectively. For comparison, the coral-like N-doped carbon materials (referred to as N-CP-X) were also prepared by the same procedure described above for Co₃O₄/N-CP-X, except for addition cobalt nitrate during the hydrothermal process.

Structural and microstructural analyses of Co₃O₄/N-CP-X. Fig. 2a–c showed the SEM images of Co₃O₄/N-CP-900, Fig. 2d–f showed the TEM images of Co₃O₄/N-CP-900, Fig. S3a–d showed the SEM images of coral-like polyaniline and Co₃O₄/PANI, Fig. S4a–d showed the SEM images of Co₃O₄/N-CP-800 and Co₃O₄/N-CP-1000. As shown in Fig. 2, Figs S3 and S4, all of samples displayed a well-developed, defined coral-like 3D morphology and the coral-like structure of Co₃O₄/N-CP-X sample maintained after hydrothermal reaction and pyrolysis. Co₃O₄/N-CP-900 displayed a uniform and coral-like structure with a diameter of 3 μm that was composed of nanofibers with diameter ca. 180 nm (Fig. 2a–c). TEM image also confirms the above results (Fig. 2d), showed a coral-like radial structure, which is beneficial to increase the specific surface area and provide more active sites. The enlarged TEM image showed that the carbon nanotubes structures decorated some Co₃O₄ nanoparticles with a diameter range about from 10–50 nm (Fig. 2e). The morphology of Co₃O₄/N-CP-900 was further studied using high resolution transmission electron microscopy (HRTEM). The HRTEM image showed that the nanoparticles decorated on carbon nanotubes (Fig. 2f), simultaneously exhibiting a spacing of

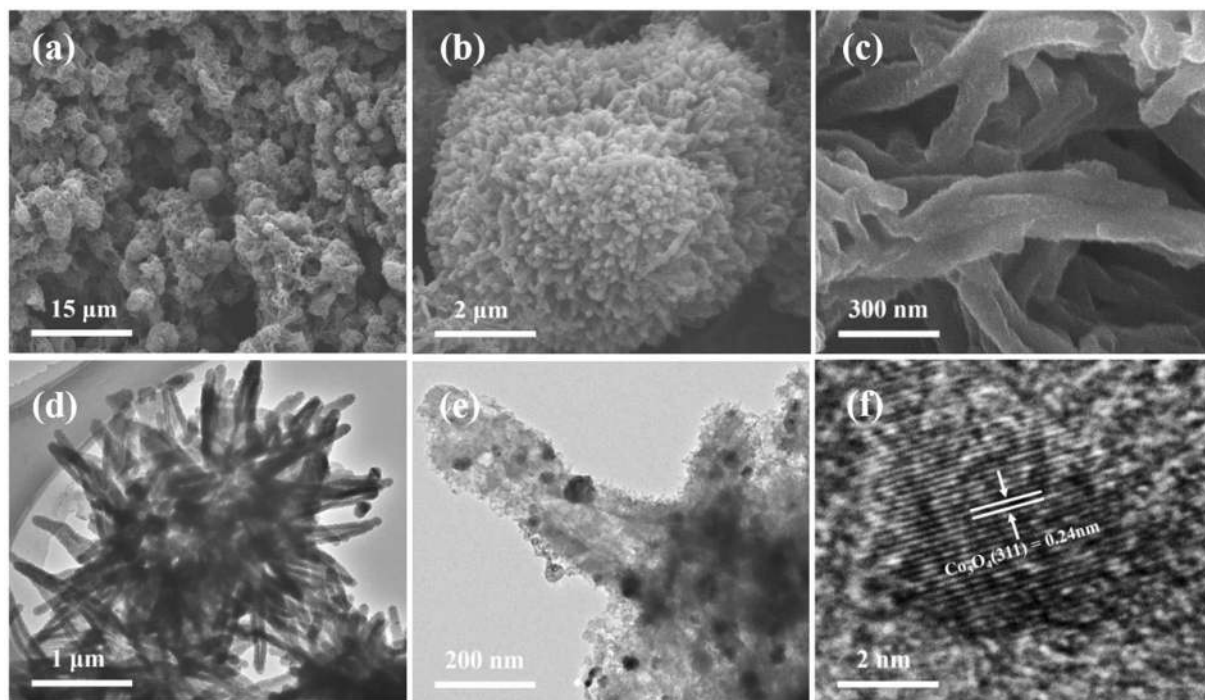


Figure 2. (a–c) SEM images, (d–e) TEM images, and (f) HRTEM images of coral-like $\text{Co}_3\text{O}_4/\text{N-CP-900}$.

crystalline lattices of 0.24 nm and corresponding to the Co_3O_4 phase [311] planes²⁴, which indicated high crystallinity of cobalt oxide nanocrystal.

The scanning transmission electron microscopy (STEM) image of the coral-like $\text{Co}_3\text{O}_4/\text{N-CP-900}$ and the corresponding energy dispersive X-ray spectroscopy (EDS) elemental mapping were given in Fig. 3. STEM bright-field image (Fig. 3a) suggested that the black nanoparticles were decorated on carbon nanotubes. The EDS mapping of C, N, O and Co were shown in Fig. 3c–f, corresponding to the STEM bright-field image, further indicated that many cobalt oxide nanoparticles were decorated on carbon nanotubes of coral-like $\text{Co}_3\text{O}_4/\text{N-CP-900}$, thus providing a high density of active sites. The EDS elemental mappings of N confirmed a uniform distribution of N atoms in coral-like $\text{Co}_3\text{O}_4/\text{N-CP-900}$ particles, which is important to promote the electrocatalytic efficiency for ORR and supercapacitor. The above results verified that the Co_3O_4 nanoparticles anchored on N-doped carbon nanomaterials might enhance electrochemical stability of coral-like $\text{Co}_3\text{O}_4/\text{N-CP-900}$ for ORR and supercapacitor. Furthermore, the anchored metal oxide nanoparticles could generate a unique host-guest electronic interaction and change the local work function of the carbon, making the outer surface of the carbon layer more active to ORR²⁵.

The coral-like $\text{Co}_3\text{O}_4/\text{N-CP-X}$ materials were investigated by Brunauer-Emmett-Teller (BET) surface area, pore size distribution, Raman spectroscopy, X-ray photoelectron spectroscopy (XPS), X-ray diffraction (XRD). Brunauer-Emmett-Teller (BET) surface area and pore size distribution were investigated by a N_2 adsorption-desorption analysis, as shown in Fig. 4a,b. All the coral-like $\text{Co}_3\text{O}_4/\text{N-CP-X}$ catalysts show the type I isotherm in Fig. 4a, manifesting they are the properties of microporous materials¹⁷. The $\text{Co}_3\text{O}_4/\text{N-CP-900}$ exhibited the higher BET surface area of $738.3 \text{ m}^2 \text{ g}^{-1}$ than $621.4 \text{ m}^2 \text{ g}^{-1}$ for $\text{Co}_3\text{O}_4/\text{N-CP-800}$, and $449.5 \text{ m}^2 \text{ g}^{-1}$ for $\text{Co}_3\text{O}_4/\text{N-CP-1000}$. It can be concluded that increasing treatment temperature from 800 to 900 °C significantly increase the specific surface area, but further increasing temperature leads to a slight decrease in the specific surface area, which may be attributed to the partial destruction of ordered micropores^{18,19}. It could be considered that the high surface area materials would introduce more active sites, thereby enhancing the catalytic ORR activity and supercapacitor performance. The porous structures were observed in the pore size distribution curves of $\text{Co}_3\text{O}_4/\text{N-CP-X}$ (Fig. 4b). Barrett-Joyner-Halenda (BJH) desorption average pore diameter for $\text{Co}_3\text{O}_4/\text{N-CP-800}$, $\text{Co}_3\text{O}_4/\text{N-CP-900}$ and $\text{Co}_3\text{O}_4/\text{N-CP-1000}$ were found to be 0.5, 0.6 and 0.4 nm, respectively. The peak below 1 nm observed in the pore size distribution curves for all the materials further pointed towards the majority of micropores, which facilitates oxygen adsorption and desorption, as well as exposure to active sites and rapid ion and electrolyte transport.

As shown in Fig. 4c, the Raman spectra of coral-like $\text{Co}_3\text{O}_4/\text{N-CP-X}$ displayed two bands; D band and G band at $1,335 \text{ cm}^{-1}$ and $1,580 \text{ cm}^{-1}$, respectively, corresponding with the disordered graphitic carbon and the vibration of the sp^2 -bonded carbon atoms in the two-dimensional hexagonal lattice, which indicated the formation of graphite carbon during pyrolysis^{19,26}. The integrated intensity ratio of the D and G band (I_D/I_G) is widely used to assess the graphite material defect density^{19,26}. The I_D/I_G values of $\text{Co}_3\text{O}_4/\text{N-CP-800}$ was 1.23, $\text{Co}_3\text{O}_4/\text{N-CP-900}$ was 1.21, and $\text{Co}_3\text{O}_4/\text{N-CP-1000}$ was 1.18, respectively, indicating that the graphitization degree of $\text{Co}_3\text{O}_4/\text{N-CP-X}$ was improved with the increasing pyrolysis temperature. As presented in XRD patterns of Fig. S5f, the peaks are due to those of the monoclinic phase of Co_3O_4 , which is correspond to the result of TEM.

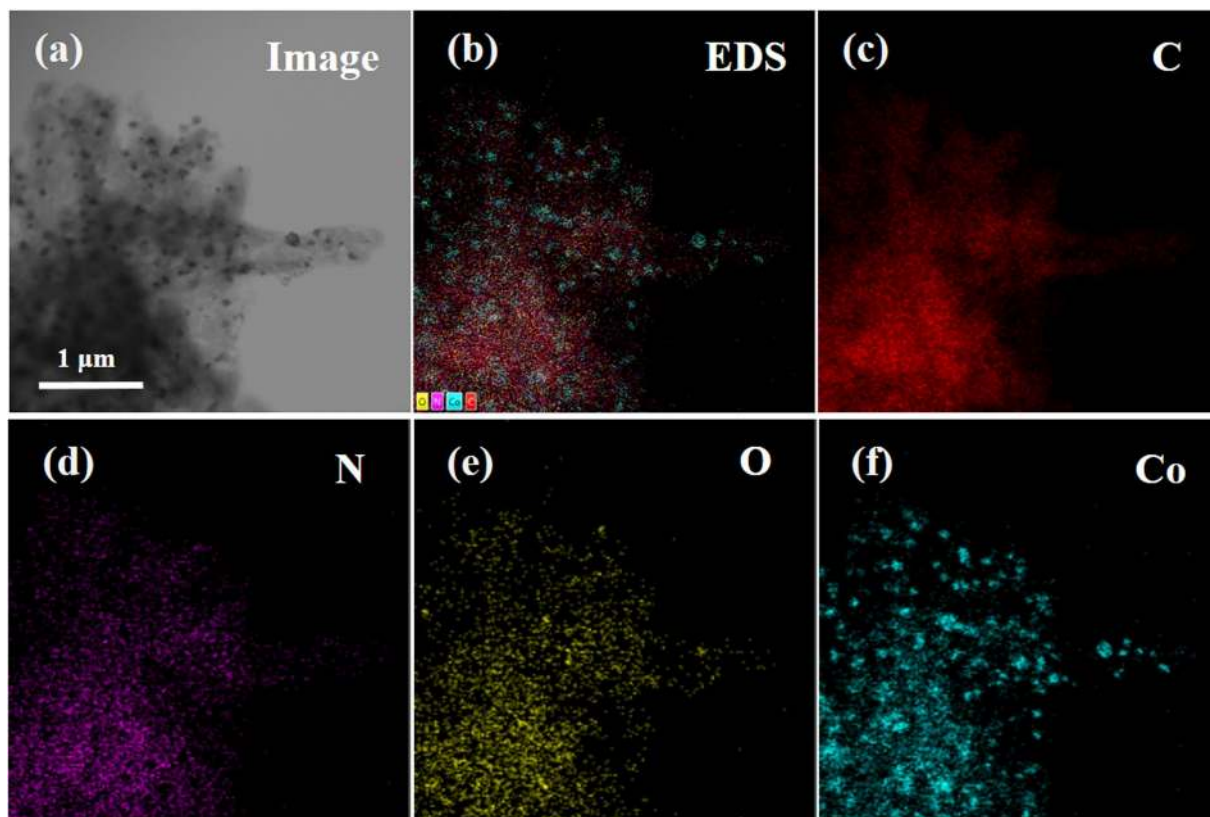


Figure 3. STEM and the corresponding elemental mapping images of coral-like $\text{Co}_3\text{O}_4/\text{N-CP-900}$ indicating the distribution of C, N, O and Co elements.

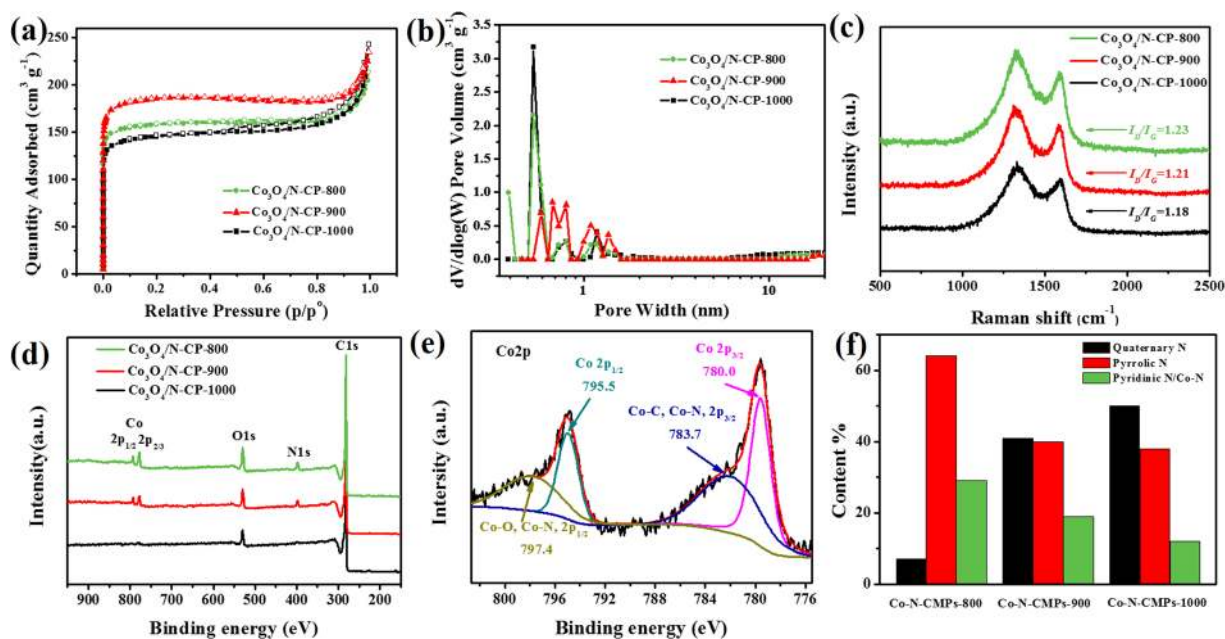


Figure 4. (a) N_2 adsorption-desorption isotherm of the $\text{Co}_3\text{O}_4/\text{N-CP-X}$, (b) Corresponding pore size distribution curves of the $\text{Co}_3\text{O}_4/\text{N-CP-X}$, (c) Raman (λ_{ex} at 633 nm) spectra of the $\text{Co}_3\text{O}_4/\text{N-CP-X}$, (d) XPS survey spectra of the $\text{Co}_3\text{O}_4/\text{N-CP-X}$, (e) High-resolution $\text{Co}2p$ XPS spectrum of the $\text{Co}_3\text{O}_4/\text{N-CP-900}$, (f) The N species distribution of the $\text{Co}_3\text{O}_4/\text{N-CP-900}$.

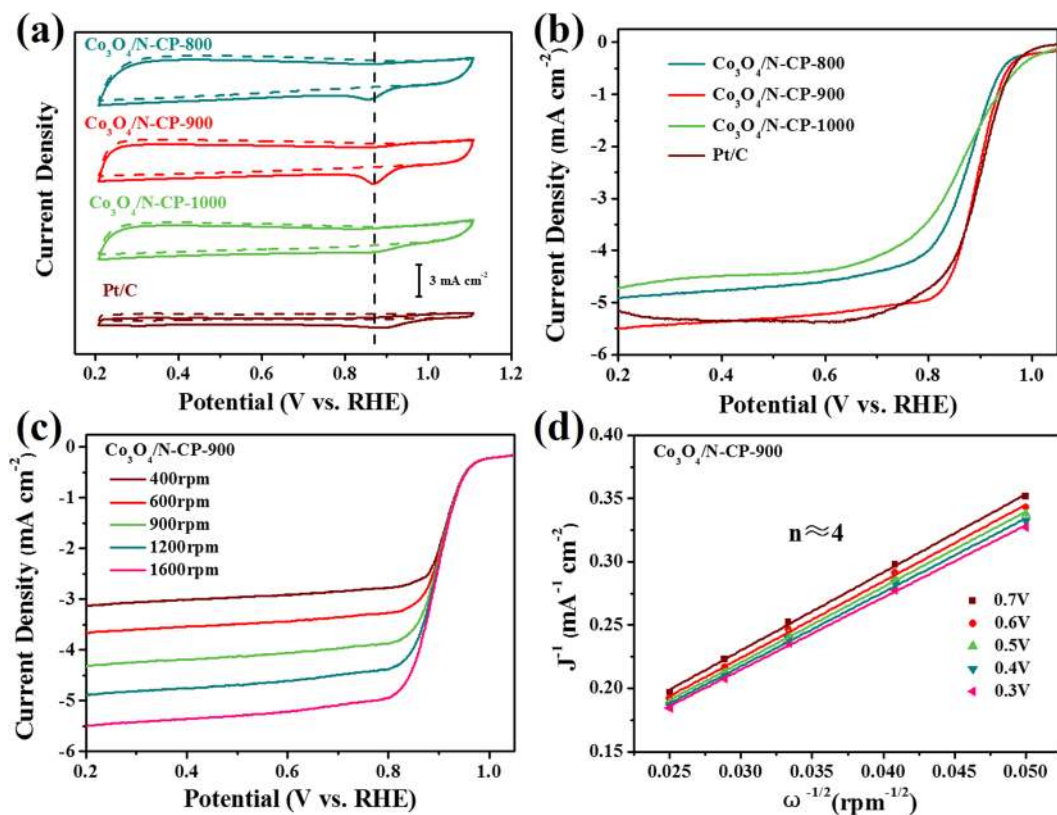


Figure 5. (a) CV curves of $\text{Co}_3\text{O}_4/\text{N-CP-800}$, $\text{Co}_3\text{O}_4/\text{N-CP-900}$, $\text{Co}_3\text{O}_4/\text{N-CP-1000}$ and commercial Pt/C in N_2 (dotted lines) and O_2 -saturated (solid lines) 0.1 M KOH solution with a scan rate of 50 mV s^{-1} . (b) LSV curves of $\text{Co}_3\text{O}_4/\text{N-CP-800}$, $\text{Co}_3\text{O}_4/\text{N-CP-900}$, $\text{Co}_3\text{O}_4/\text{N-CP-1000}$ and commercial Pt/C in O_2 -saturated 0.1 M KOH solution at a rotation rate of 1600 rpm with a scan rate of 10 mV s^{-1} . (c,d) LSV curves and related K-L plots of $\text{Co}_3\text{O}_4/\text{N-CP-900}$ in O_2 -saturated 0.1 M KOH solution with a scan rate of 10 mV s^{-1} at different rotation rates from 400 to 1600 rpm.

The survey XPS spectra of coral-like $\text{Co}_3\text{O}_4/\text{N-CP-X}$ showed the presence of C, O, N and Co elements (Fig. 4d), indicating that the carbon framework was successfully doped with nitrogen. We found that the nitrogen content was reduced by increasing the pyrolysis temperature due to the loss of unstable nitrogen. Nitrogen contents in $\text{Co}_3\text{O}_4/\text{N-CP-800}$, $\text{Co}_3\text{O}_4/\text{N-CP-900}$ and $\text{Co}_3\text{O}_4/\text{N-CP-1000}$ were 3.37 at %, 2.10 at % and 1.39 at %, respectively. Fig. S5a–c displayed N1s XPS spectra of the as-prepared $\text{Co}_3\text{O}_4/\text{N-CP-800}$, $\text{Co}_3\text{O}_4/\text{N-CP-900}$ and $\text{Co}_3\text{O}_4/\text{N-CP-1000}$, respectively. Deconvolution of the N1s XPS spectrum was performed with three peaks corresponding to pyridinic N (398.5 eV), pyrrolic N (400.3 eV) and graphitic-type quaternary N (401.5 eV)²⁷. Since the difference between the binding energy of Co-N and pyridinic N is very small, the peak centered at 398.5 eV also includes the contribution of N bond to cobalt (Co-N)²⁸. The relative N specie distributions in $\text{Co}_3\text{O}_4/\text{N-CP-X}$ were compared in Fig. 4f. The ratios of graphitic-type quaternary N, pyrrolic N and pyridinic N were 7%, 64% and 29% in $\text{Co}_3\text{O}_4/\text{N-CP-800}$, respectively, 41%, 40% and 19% for $\text{Co}_3\text{O}_4/\text{N-CP-900}$, respectively, 50%, 38%, and 12% for $\text{Co}_3\text{O}_4/\text{N-CP-1000}$, respectively. These results show that the proportions of graphitic-type quaternary N increased with increasing temperature, and the proportion of pyrrolic N decreased due to its instability. Research shows that the content of graphitic-type quaternary N determines the limiting current density, while the pyridinic N content increased the ORR onset potential²⁹. Pyridinic N contribute a *p*-electron to the aromatic *p*-system and has a single electron pair in the plane of carbon matrix, which can improve the electron donating ability. Thus, it weakens the O-O bond by bonding oxygen with nitrogen and/or adjacent carbon atoms, which facilitates the reduction of O_2 ³⁰. The optimum oxygen reduction performance of the $\text{Co}_3\text{O}_4/\text{N-CP-900}$ is due to the high content of graphitic-type quaternary N and pyridinic N^{31,32}. The C1s XPS spectrum of $\text{Co}_3\text{O}_4/\text{N-CP-900}$ (Fig. S5d) can be deconvoluted into three peaks corresponding to graphene (284.0 eV)³³, C-N (285.0 eV) and carboxyl C=O (288.4 eV) carbon bonded with oxygen, which corresponded to the O1s peak (Fig. S5e). The Co2p XPS spectrum of the $\text{Co}_3\text{O}_4/\text{N-CP-900}$ was given in Fig. 4e, and the data showed two major peaks at 780.0 (795.5) and 783.7 (797.4) eV corresponding to the Co and cobalt compounds (Co-O or Co-N)^{34,35}. Taken together, we deduced that $\text{Co}_3\text{O}_4/\text{N-CP-X}$ catalysts were composed of Co_3O_4 decorated N-doped carbon.

Characterization by cyclic voltammetry. The ORR electrocatalytic activities of coral-like $\text{Co}_3\text{O}_4/\text{N-CP-X}$ and commercial Pt/C catalysts were evaluated by cyclic voltammetry (CV). As seen in Fig. 5a, all catalysts showed a quasi-rectangular voltammograms (dashed lines) without a redox peak over the potential range of 0.2 to 1.1 V in the N_2 -saturated solution. In the O_2 -saturated solution, the $\text{Co}_3\text{O}_4/\text{N-CP-900}$ catalysts observed an ORR

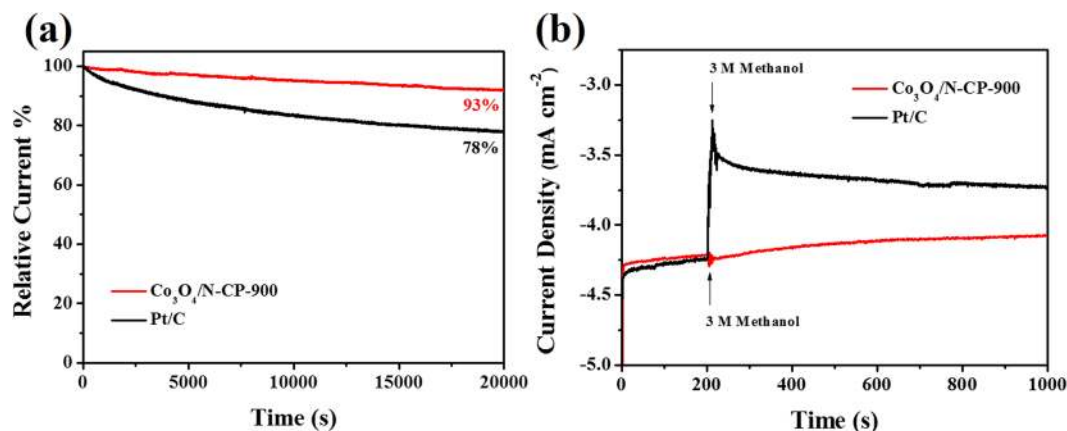


Figure 6. (a) Chrono-amperometric current-time (*i*-*t*) curves of $\text{Co}_3\text{O}_4/\text{N-CP-900}$ and commercial Pt/C in O_2 -saturated 0.1 M KOH solution at 0.4 V. b) Chrono-amperometric responses of $\text{Co}_3\text{O}_4/\text{N-CP-900}$ and commercial Pt/C at 0.4 V to adding 3.0 M methanol into O_2 -saturated 0.1 M KOH solution.

reduction with peak potential at 0.88 V (vs. RHE), which was more positive than $\text{Co}_3\text{O}_4/\text{N-CP-800}$ (0.85 V) and $\text{Co}_3\text{O}_4/\text{N-CP-1000}$ (0.86 V), basically compared to Pt/C catalyst (0.90 V). Moreover, the $\text{Co}_3\text{O}_4/\text{N-CP-900}$ exhibited a higher peak current density (4.32 mA cm^{-2}) than Pt/C catalyst (1.66 mA cm^{-2}). The CV curves of N-CP-900 without Co_3O_4 were also measured for comparison. The CV curves in Fig. S6a show obvious oxygen reduction peak for N-CP-900 at 0.81 V. It is found that $\text{Co}_3\text{O}_4/\text{N-CP-900}$ exhibit a higher active than N-CP-900 catalyst, due to combination of cobalt oxide with N-doped carbon, which prove that Co species plays a key role in improving ORR performance. The above results showed that coral-like $\text{Co}_3\text{O}_4/\text{N-CP-900}$ catalyst is a high performance ORR electrocatalyst.

Electrocatalytic reduction of oxygen. Then, we measured the linear sweep voltammogram (LSV) at a rotation rate of 1600 rpm on a rotating disk electrode (RDE). The LSV curves of $\text{Co}_3\text{O}_4/\text{N-CP-900}$ displayed the onset and half-wave potentials of 0.97 and 0.90 V in Fig. 5b, which was more positive than $\text{Co}_3\text{O}_4/\text{N-CP-800}$ (0.96 V and 0.87 V), $\text{Co}_3\text{O}_4/\text{N-CP-1000}$ (0.98 V and 0.86 V) and N-CP-900 (0.89 and 0.85 V) (Fig. S6b), and very similar to Pt/C catalyst (0.99 V and 0.89 V). The limited current density of $\text{Co}_3\text{O}_4/\text{N-CP-900}$ (5.50 mA cm^{-2}) was comparable to Pt/C catalyst (5.15 mA cm^{-2}). The ORR performances of cobalt/nitrogen-codoped carbon materials are summarized in Table S1. Compared with other reports, $\text{Co}_3\text{O}_4/\text{N-CP-900}$ exhibit excellent ORR performance, with more positive onset and half-wave potential, as well as a high diffusion-limited current density. In summary, these results indicate that the coral-like $\text{Co}_3\text{O}_4/\text{N-CP-900}$ catalyst exhibits excellent ORR catalytic activity, which can be used as a promising candidate material for commercial Pt/C catalysts.

LSV curves of $\text{Co}_3\text{O}_4/\text{N-CP-900}$, $\text{Co}_3\text{O}_4/\text{N-CP-800}$, $\text{Co}_3\text{O}_4/\text{N-CP-1000}$ and commercial Pt/C catalyst in O_2 -saturated 0.1 M KOH at different rotation rate were shown in Fig. 5c and Fig. S7a-c. RDE measured showed that the electron transfer number was close to 4.0 at 0.3–0.7 V on the basis of the Koutecky-Levich (K-L) plots (Fig. 5d, Fig. S7d-f). Compared to $\text{Co}_3\text{O}_4/\text{N-CP-800}$ and $\text{Co}_3\text{O}_4/\text{N-CP-1000}$, $\text{Co}_3\text{O}_4/\text{N-CP-900}$ was closer to a 4-electron transfer process toward ORR.

The stability of the catalyst is also a problem to be considered for ORR. We accelerated the degradation of $\text{Co}_3\text{O}_4/\text{N-CP-900}$ catalyst using the current-time (*i*-*t*) method. $\text{Co}_3\text{O}_4/\text{N-CP-900}$ catalyst exhibits such excellent durability, that it still has a high retention of 93% compared to the initial current even after 20000 s test, while only 78% of the commercial Pt/C catalyst was retained (Fig. 6a). In addition, we also tested the methanol tolerance of $\text{Co}_3\text{O}_4/\text{N-CP-900}$ catalyst, compared with commercial Pt/C catalyst. The current density of the $\text{Co}_3\text{O}_4/\text{N-CP-900}$ catalyst remained almost constant after the addition of 3 M methanol, whereas the commercial Pt/C catalyst showed a significant current change (Fig. 6b). In conclusion, coral-like $\text{Co}_3\text{O}_4/\text{N-CP-900}$ catalyst have higher stability and better methanol tolerance than commercial Pt/C catalyst.

Electrochemical performance of supercapacitor. Except for the ORR catalyst, the coral-like $\text{Co}_3\text{O}_4/\text{N-CP-X}$ material can be used as an electrode material for the energy storage device. We explored supercapacitor performance by assemble symmetrical two-electrode cell. Fig. 7a showed a typical CVs of a $\text{Co}_3\text{O}_4/\text{N-CP-900}$ electrode with a scanning rate of 10 to 100 mV s^{-1} at the potential range of -0.8 to 0.2 V in 6 M KOH aqueous solution, which was close to the rectangle, implying the characteristics of carbon based supercapacitors³⁶. As the specific capacitance increases with current density, so the CV curve area is proportional to the specific capacitance. With the increase of scan rate, there is no obvious change of CV curves, indicating that the $\text{Co}_3\text{O}_4/\text{N-CP-900}$ electrode has fast charge and discharge performance³⁷. At the same time, we compared the performance of samples obtained at different pyrolysis temperatures. The internal area of CV curve for $\text{Co}_3\text{O}_4/\text{N-CP-900}$ was enlarged compared to that of $\text{Co}_3\text{O}_4/\text{N-CP-800}$ and $\text{Co}_3\text{O}_4/\text{N-CP-1000}$, indicating that the specific capacitance of $\text{Co}_3\text{O}_4/\text{N-CP-900}$ is higher than that of $\text{Co}_3\text{O}_4/\text{N-CP-800}$ and $\text{Co}_3\text{O}_4/\text{N-CP-1000}$ (Fig. S8a). As can be seen from Fig. 7b, the galvanostatic charge and discharge curves were almost triangular, which approximated the ideal supercapacitors behavior. The results showed that the high specific surface area and pore volume of $\text{Co}_3\text{O}_4/\text{N-CP-900}$ results in excellent supercapacitor performance. As shown in Fig. 7c, the

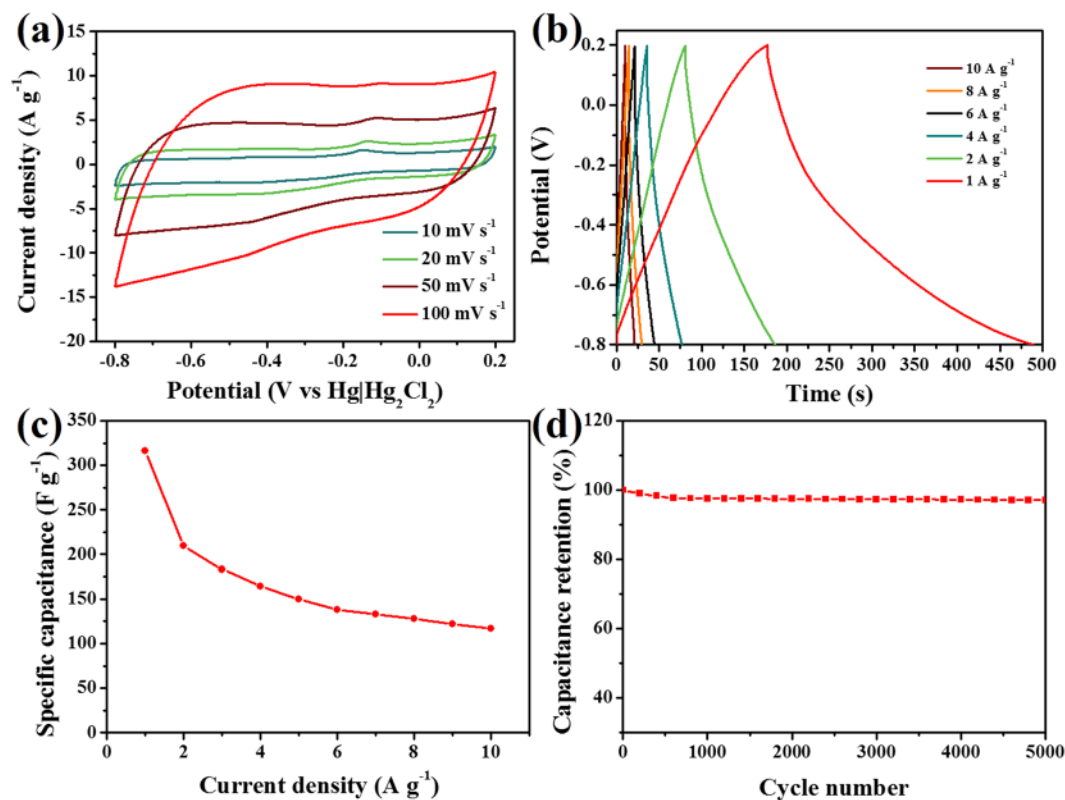


Figure 7. Electrochemical performance of supercapacitor by using a $\text{Co}_3\text{O}_4/\text{N-CP-900}$ electrode with a two-electrode system: (a) Cyclic voltammetry curves and (b) galvanostatic charge/discharge curves by using 6 M KOH as electrolyte, (c) Relationship between specific capacitances (C_s) and current density, (d) Cycling stability of $\text{Co}_3\text{O}_4/\text{N-CP-900}$ at 5.0 A g^{-1} in 6 M KOH.

specific capacitance (C_s) at 1.0 A g^{-1} in the 6 M KOH aqueous solution was calculated to be 316.2 F g^{-1} by the galvanostatic discharge curve, and the C_s values also reached 117.1 F g^{-1} even at the current density of 10 A g^{-1} . The microporous structure results in high specific surface area and pore volume, leading to $\text{Co}_3\text{O}_4/\text{N-CP-900}$ with a good capacitance. Specific capacitances are 225.5, 316.2 and 174.6 F g^{-1} at a current density of 1.0 A g^{-1} for the samples $\text{Co}_3\text{O}_4/\text{N-CP-800}$, $\text{Co}_3\text{O}_4/\text{N-CP-900}$ and $\text{Co}_3\text{O}_4/\text{N-CP-1000}$, respectively (Fig. S8b). The results were consistent with the area of CV curves. As the pyrolysis temperature increases, the specific surface area of the electrode material increases gradually, resulting in a higher specific capacitance of $\text{Co}_3\text{O}_4/\text{N-CP-900}$ than that of $\text{Co}_3\text{O}_4/\text{N-CP-800}$. However, the specific capacitance of $\text{Co}_3\text{O}_4/\text{N-CP-1000}$ is significantly lower than that of $\text{Co}_3\text{O}_4/\text{N-CP-900}$, which is due to the too high pyrolysis temperature, causing the electrode material to form clumps and the electrolyte unable to penetrate into the electrode material. We also performed galvanostatic charge and discharge tests at a current density of 5 A g^{-1} to evaluate the durability of the $\text{Co}_3\text{O}_4/\text{N-CP-900}$ electrode. After 5000 cycles of charge and discharge, a high capacity retention of 90% was achieved, showing good cycle performance (Fig. 7d). The excellent performance of $\text{Co}_3\text{O}_4/\text{N-CP-900}$ electrode is due to the uniform N doping and Co_3O_4 anchoring effect, which improves the conductivity, wettability and reactivity of the materials.

In addition, we characterized the electrochemical impedance spectroscopy (EIS) of $\text{Co}_3\text{O}_4/\text{N-CP-800}$, $\text{Co}_3\text{O}_4/\text{N-CP-900}$ and $\text{Co}_3\text{O}_4/\text{N-CP-1000}$ at room temperature. The Nyquist plot of $\text{Co}_3\text{O}_4/\text{N-CP-900}$ electrode was obtained in 6 M KOH aqueous solution (Fig. 8). From the high-frequency end of the Nyquist plot x intercept can be 0.75Ω resistance, which is almost the resistance of the electrolyte³⁸. $\text{Co}_3\text{O}_4/\text{N-CP-900}$ showed a smaller kinetic arc at high-frequencies than that of $\text{Co}_3\text{O}_4/\text{N-CP-800}$ and $\text{Co}_3\text{O}_4/\text{N-CP-1000}$, which means that its charge transfer resistance was relatively lower than that of $\text{Co}_3\text{O}_4/\text{N-CP-800}$ and $\text{Co}_3\text{O}_4/\text{N-CP-1000}$, indicating that the charge transfer efficiency of $\text{Co}_3\text{O}_4/\text{N-CP-900}$ was high. The low frequency stimulation of the EIS spectrum of $\text{Co}_3\text{O}_4/\text{N-CP-900}$ was almost vertical, which indicated that the ions rapidly diffused in the electrolyte during charge and discharge¹⁴. This shows that $\text{Co}_3\text{O}_4/\text{N-CP-900}$ is closer to the ideally capacitive behavior than $\text{Co}_3\text{O}_4/\text{N-CP-800}$ and $\text{Co}_3\text{O}_4/\text{N-CP-1000}$. The above test results show that the supercapacitor with $\text{Co}_3\text{O}_4/\text{N-CP-900}$ electrode has extremely low internal resistance. We conclude that the good electrochemical performance of coral-like $\text{Co}_3\text{O}_4/\text{N-CP-900}$ electrode can be attributed to the combined effect of high specific surface area, narrow pore size distribution and heteroatom doping. The interconnected microporous structure allows the electrolyte to pass more efficiently and reduces the resistance within the electrode. Moreover, heteroatom doping can increase the surface wettability, pseudocapacitance, chemical stability and conductivity of carbon materials.

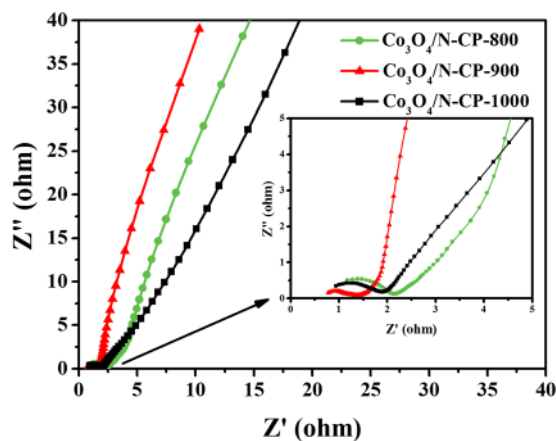


Figure 8. Electrochemical impedance spectrum of the $\text{Co}_3\text{O}_4/\text{N-CP-800}$, $\text{Co}_3\text{O}_4/\text{N-CP-900}$ and $\text{Co}_3\text{O}_4/\text{N-CP-1000}$ electrode in 6 M KOH electrolyte. The inset shows the magnified electrochemical impedance spectrum in a high-frequency range.

Conclusions

In summary, a coral-like $\text{Co}_3\text{O}_4/\text{N-CP}$ with high electrochemical performances toward ORR and supercapacitor electrode in alkaline media was fabricated by chemical polymerization of aniline, hydrothermal, and pyrolysis. $\text{Co}_3\text{O}_4/\text{N-CP-900}$ showed a positive onset potential of 0.97 V, half-wave potential of 0.90 V, as well as a high diffusion-limited current density of 5.50 mA cm^{-2} in 0.1 M KOH. Compared to Pt/C catalysts, it also exhibits good stability and excellent methanol tolerance. In addition, $\text{Co}_3\text{O}_4/\text{N-CP-900}$ electrode exhibited an excellent specific capacitance of 316.2 F g^{-1} in 6 M KOH aqueous solution at a current density of 1.0 A g^{-1} , as well as good rate capabilities and high cycling stabilities. The good activity of ORR and supercapacitors is due to the high specific surface area and microporous structure, which not only improves the availability of electron transport within the surface area, but also allows the reactants to be better delivered. With the decoration of Co_3O_4 on N-doped carbon, the ORR catalytic activity could be improved significantly due to a high density of active sites. This work may provide an approach to develop transition metal oxide decorated nitrogen co-doped carbon materials as advanced catalysts for use in electrochemical energy conversion and storage.

Methods

Materials. Aniline was purchased from Aladdin, and distilled before use. Perfluorosebacic acid was purchased from TCI(Shanghai) Development Co., Ltd. $\text{Co}(\text{NO}_3)_2 \cdot 6\text{H}_2\text{O}$, KOH, ammonium persulfate, methanol, and ether were purchased from Beijing Beihua Fine Chemicals Co., Ltd. Commercial carbon-supported Pt catalyst (20 wt.%, Pt/C) was purchased from Sigma-Aldrich. Nafion (DuPont, 10 wt.%) was diluted to 0.05 wt% using ethanol.

Synthesis of coral-like Co_3O_4 decorated N-doped carbon particles ($\text{Co}_3\text{O}_4/\text{N-CP}$). First, 20 mL of 0.025 mol L^{-1} perfluorodecanoic acid (PFSEA) aqueous solution was prepared, and then 4 mmol aniline was added to form a uniform emulsion under ultrasonic action. Subsequently, 20 mL of 0.2 mol L^{-1} ammonium persulfate (APS) aqueous solution was added to the above uniform emulsion and reacted at 12°C for 15 hours. In order to completely remove the by-product, the obtained polyaniline was washed with methanol, ether and deionized water, then filtered and dried to obtain coral-shaped polyaniline (PANI) nanoparticles. $\text{Co}_3\text{O}_4/\text{PANI}$ was prepared by hydrothermal method, as reported previously²³. The obtained polyaniline was added to 40 mL deionized water under ultrasonic conditions, and 4 mmol $\text{Co}(\text{NO}_3)_2 \cdot 6\text{H}_2\text{O}$ was added to the above solution. After 30 min of sonication, the mixture was added to a 50 mL polytetrafluoroethylene liner stainless autoclave, then heated at 180°C for 24 h. The $\text{Co}_3\text{O}_4/\text{PANI}$ was collected by centrifugation and washed with deionized water and ethanol. Finally, the materials were prepared by pyrolyzing the precursors at 800°C , 900°C , 1000°C in a nitrogen atmosphere for 3.0 h at a heating rate of $5^\circ\text{C}/\text{min}$. The final product was denoted as $\text{Co}_3\text{O}_4/\text{N-CP-X}$ (X represents temperature). For comparison, the metal-free carbon catalyst (referred to as N-CP-X) was also prepared by the same procedure as that of $\text{Co}_3\text{O}_4/\text{N-CP-X}$, except that cobalt nitrate was removed during the hydrothermal reaction.

Characterization. The microstructure of the $\text{Co}_3\text{O}_4/\text{N-CP-X}$ were observed by field emission scanning electron microscope (FESEM) (JEOL JSM-7500F), environmental scanning electron microscopy (ESEM) (Quanta 250 FEG) and field emission transmission electron microscope (TEM) (JEOL JEM-2100F). X-ray diffraction (XRD) were conducted using the PANalytical, Empyrean XRD (CuK α 1.5406 Å radiation), and the surface chemical composition of the $\text{Co}_3\text{O}_4/\text{N-CP-X}$ was obtained by the X-ray photoelectron spectroscopy (XPS) (VG ESCALAB 220i-XL photoelectron spectrometer with a monochromatic AlK α X-ray source). The surface area (BET) and pore size distribution (BJH) were performed on Micromeritics ASAP 2020 V3.00 H system. The Raman spectra was recorded on a Laboratory RAM HR1800.

Oxygen reduction reaction measurements. Oxygen reduction reaction properties were measured using a three-electrode system on the CHI 760D (Chenhua, Shanghai) electrochemical workstation. Preparation of working electrode by weighing 2 mg of catalyst into 1 mL of ethanol solution, ultrasonic 20 min, forming a highly dispersed catalyst solution (2 mg mL⁻¹). Take 15 μ L of the catalyst ethanol solution into the rotating disk electrode (RDE, disc diameter 3 mm) surface, room temperature drying, and then dropping 7.5 μ L 0.05% Nafion ethanol solution, room temperature drying. Among them, the platinum wire and the saturated Hg|Hg₂Cl₂ (KCl sat.) were used as the counter electrode and the reference electrode, respectively, and the rotating disk electrode with the catalyst was used as the working electrode. The cyclic voltammetry (CV) tests were carried out in O₂-saturated and N₂-saturated 0.1 mol L⁻¹ KOH solution with a scanning rate of 50 mV s⁻¹ at a test potential ranging from -0.8 V to 0.1 V, and linear sweep voltammetry (LSV) tests at a scanning rate of 10 mV s⁻¹ at different rotational rates of 400, 600, 900, 1200 and 1600 rpm in 0.1 mol L⁻¹ KOH solution saturated with O₂. All tests were carried out in a 25 °C thermostatic system.

The number of electrons transferred in the ORR process (n) is determined using the Koutecky-Levich (K-L) (1):

$$\frac{1}{J} = \frac{1}{J_K} + \frac{1}{J_L} = \frac{1}{J_K} + \frac{1}{B\omega^{1/2}}$$

$$B = 0.2 nFC_{O_2}(D_{O_2})^{2/3}v^{-1/6} \quad (1)$$

Here, J , J_K and J_L are the measured current density, kinetic current density and diffusion-limited current density, respectively, ω is the rotation rate, B can be determined by the slope of K-L plots based on the Levich equation, n is the number of electrons transferred per oxygen molecule, F is the Farady constant (96485 C mol⁻¹), C_{O_2} is the bulk concentration of O₂ in 0.1 mol L⁻¹ KOH (1.2 $\times 10^{-6}$ mol cm⁻³), D_{O_2} is the diffusion coefficient of O₂ in 0.1 mol L⁻¹ KOH (1.9 $\times 10^{-5}$ cm² s⁻¹) and v is the kinetic viscosity (1.10 $\times 10^{-2}$ cm² s⁻¹)^{39,40}.

The electrode stability at the bias potential of 0.8 V (vs. RHE) in O₂-saturated 0.1 M KOH solutions using current-time (i-t) method with a rotation rate of 1000 rpm. Then, 5 mL methanol is added to the O₂-saturated 0.1 M KOH aqueous solution to test the tolerance to methanol crossover effect.

Supercapacitor measurements. Supercapacitor properties were measured using a three electrode cell on the CHI 760E (Chenhua, Shanghai) electrochemical workstation. For capacitance measurements, the Co₃O₄/N-CP-900 particles, polyvinylidene fluoride, and carbon black were mixed at a weight ratio 8:1:1 in N-Methyl-2-pyrrolidone solvent as the working electrode. The mixture was firstly well mixed to form a slurry and it was coated onto a piece of carbon paper (1 \times 1 cm²), and dried for 12 h at 120 °C. The CV test at a scan rate of 10 to 100 mV s⁻¹. Measure galvanostatic charge and discharge to evaluate specific capacitance and cyclability. The cells were charged/discharged at current rates ranging from 1 to 10 A g⁻¹ for 10 cycles to measure the capacitance. The cells were charged/discharged at a current density of 5 A g⁻¹ for 5000 cycles to tests the cyclability. The equation is used to calculate the specific capacitance (C_s) of the electrode material (2):

$$C_s = \frac{I\Delta t}{\Delta Vm} \quad (2)$$

Here, I , Δt and m are the discharge current, discharge time and mass of carbon on the electrode, respectively, ΔV is the voltage difference within Δt . At the open circuit voltage, electrochemical impedance spectroscopy (EIS) test in the 10 mHz to 100 kHz frequency range, the amplitude of 5 mV. According to the constant current discharge process with different current density, the ragone diagram was calculated^{38,41}.

References

- Debe, M. K. Electrocatalyst approaches and challenges for automotive fuel cells. *Nature* **486**, 43–51 (2012).
- Steele, B. C. H. & Heinze, A. review article Materials for fuel-cell technologies. *Nature* **414**, 345–352 (2001).
- Huang, X. *et al.* High-performance transition metal-doped Pt₃Ni octahedra for oxygen reduction reaction. *Science* **348**, 1230–1234 (2015).
- Wang, D. *et al.* Structurally ordered intermetallic platinum-cobalt core-shell nanoparticles with enhanced activity and stability as oxygen reduction electrocatalysts. *Nat. Mater.* **12**, 81–87 (2013).
- Katsounaros, I., Cherevko, S., Zeradjanin, A. R. & Mayrhofer, K. J. Oxygen electrochemistry as a cornerstone for sustainable energy conversion. *Angew. Chem. Int. Ed.* **53**, 102–121 (2014).
- Tang, C., Titirici, M. M. & Zhang, Q. A review of nanocarbons in energy electrocatalysis: Multifunctional substrates and highly active sites. *J Energy Chem.* **26**, 1077–1093 (2017).
- Dai, L., Xue, Y., Qu, L., Choi, H. J. & Baek, J. B. Metal-free catalysts for oxygen reduction reaction. *Chem. Rev.* **115**, 4823–4892 (2015).
- Cao, F. *et al.* Synthesis of Two-Dimensional CoS_{1.097}/Nitrogen-Doped Carbon Nanocomposites Using Metal-Organic Framework Nanosheets as Precursors for Supercapacitor Application. *J. Am. Chem. Soc.* **138**, 6924–6927 (2016).
- Lefevre, M., Proietti, E., Jaouen, F. & Dodelet, J. P. Iron-Based Catalysts with Improved Oxygen Reduction Activity in Polymer Electrolyte Fuel Cells. *Science* **324**, 71–74 (2009).
- Wang, B. Recent development of non-platinum catalysts for oxygen reduction reaction. *J. Power Sources.* **152**, 1–15 (2005).
- Bashyam, R. & Zelenay, P. A class of non-precious metal composite catalysts for fuel cells. *Nature* **443**, 63–66 (2006).
- Seufert, K. *et al.* Cis-dicarbonyl binding at cobalt and iron porphyrins with saddle-shape conformation. *Nat. Chem.* **3**, 114–119 (2011).
- Ania, C. O., Khomenko, V., Raymundo-Piñero, E., Parra, J. B. & Béguin, F. The Large Electrochemical Capacitance of Microporous Doped Carbon Obtained by Using a Zeolite Template. *Adv. Funct. Mater.* **17**, 1828–1836 (2007).
- Zhang, S. *et al.* Protic-salt-derived nitrogen/sulfur-codoped mesoporous carbon for the oxygen reduction reaction and supercapacitors. *ChemSusChem.* **8**, 1608–1617 (2015).
- Wu, Z. S. *et al.* 3D nitrogen-doped graphene aerogel-supported Fe₃O₄ nanoparticles as efficient electrocatalysts for the oxygen reduction reaction. *J. Am. Chem. Soc.* **134**, 9082–9085 (2012).
- Liang, Y. Y. *et al.* Oxygen reduction electrocatalyst based on strongly coupled cobalt oxide nanocrystals and carbon nanotubes. *J. Am. Chem. Soc.* **134**, 15849–15857 (2012).

17. Hao, L. *et al.* Structural evolution of 2D microporous covalent triazine-based framework toward the study of high-performance supercapacitors. *J. Am. Chem. Soc.* **137**, 219–225 (2014).
18. Xiao, M., Zhu, J., Feng, L., Liu, C. & Xing, W. Meso/macroporous nitrogen-doped carbon architectures with iron carbide encapsulated in graphitic layers as an efficient and robust catalyst for the oxygen reduction reaction in both acidic and alkaline solutions. *Adv. Mater.* **27**, 2521–2527 (2015).
19. Yang, W., Liu, X., Yue, X., Jia, J. & Guo, S. Bamboo-like Carbon Nanotube/Fe₃C Nanoparticle Hybrids and Their Highly Efficient Catalysis for Oxygen Reduction. *J. Am. Chem. Soc.* **137**, 1436–1439 (2015).
20. Pennisi, E. New Threat Seen from Carbon Dioxide. *Science*. **279**, 989–989 (1998).
21. Kleypas, J. *et al.* Geochemical consequences of increased atmospheric CO₂ on coral reefs. *Science* **284**, 118–120 (1999).
22. Warner, M. E., Fitt, W. K. & Schmidt, G. W. The effects of elevated temperature on the photosynthetic efficiency of zooxanthellae in hospite from four different species of reef coral: a novel approach. *Plant Cell Environ.* **19**, 291–299 (1996).
23. Liang, Y. *et al.* Co₃O₄ nanocrystals on graphene as a synergistic catalyst for oxygen reduction reaction. *Nat Mater.* **10**, 780–786 (2011).
24. Feng, Q., Li, X., Wang, J. & Gaskov, A. M. Reduced graphene oxide (rGO) encapsulated Co₃O₄ composite nanofibers for highly selective ammonia sensors. *Sensor Actuat B-Chem.* **222**, 864–870 (2016).
25. Chung, H. T., Won, J. H. & Zelenay, P. Active and stable carbon nanotube/nanoparticle composite electrocatalyst for oxygen reduction. *Nat. Commun.* **4**, 1922 (2013).
26. Hou, Y., Wen, Z., Cui, S., Guo, X. & Chen, J. Constructing 2D porous graphitic C₃N₄ nanosheets/nitrogen-doped graphene/layered MoS₂ ternary nanojunction with enhanced photoelectrochemical activity. *Adv. Mater.* **25**, 6291–6297 (2013).
27. Jiang, Y. *et al.* A cobalt-nitrogen complex on N-doped three-dimensional graphene framework as a highly efficient electrocatalyst for oxygen reduction reaction. *Nanoscale*. **6**, 15066–15072 (2014).
28. Wu, G. *et al.* Synthesis–structure–performance correlation for polyaniline–Me–C non-precious metal cathode catalysts for oxygen reduction in fuel cells. *J. Mater. Chem.* **21**, 11392–11405 (2011).
29. Lai, L. *et al.* Exploration of the active center structure of nitrogen-doped graphene-based catalysts for oxygen reduction reaction. *Energy Environ. Sci.* **5**, 7936–7942 (2012).
30. Zhang, J. & Dai, L. Heteroatom-Doped Graphitic Carbon Catalysts for Efficient Electrocatalysis of Oxygen Reduction Reaction. *ACS Catal.* **5**, 21–28 (2015).
31. Sheng, Z. H. *et al.* Catalyst-free synthesis of nitrogen-doped graphene via thermal annealing graphite oxide with melamine and its excellent electrocatalysis. *ACS Nano*. **5**, 4350–4358 (2011).
32. Liu, R., Wu, D., Feng, X. & Müllen, K. Nitrogen-doped ordered mesoporous graphitic arrays with high electrocatalytic activity for oxygen reduction. *Angew. Chem. Int. Ed.* **49**, 2565–2569 (2010).
33. Li, Y. *et al.* An oxygen reduction electrocatalyst based on carbon nanotube-graphene complexes. *Nat. Nanotechnol.* **7**, 394–400 (2012).
34. Pylypenko, S., Mukherjee, S., Olson, T. S. & Atanassov, P. Non-platinum oxygen reduction electrocatalysts based on pyrolyzed transition metal macrocycles. *Electrochim. Acta.* **53**, 7875–7883 (2008).
35. Ziegelbauer, J. M. *et al.* Direct spectroscopic observation of the structural origin of peroxide generation from Co-based pyrolyzed porphyrins for ORR applications. *J. Phys. Chem. C.* **112**, 8839–8849 (2008).
36. Sevilla, M., Yu, L., Ania, C. O. & Titirici, M. Supercapacitive Behavior of Two Glucose-Derived Microporous Carbons: Direct Pyrolysis versus Hydrothermal Carbonization. *ChemElectroChem.* **1**, 2138–2145 (2015).
37. Song, J. *et al.* Facile synthesis and excellent electrochemical performance of CoP nanowire on carbon cloth as bifunctional electrode for hydrogen evolution reaction and supercapacitor. *Sci China Mater.* (2017).
38. Zhang, J. & Zhao, X. S. On the configuration of supercapacitors for maximizing electrochemical performance. *ChemSusChem.* **5**, 818–841 (2012).
39. Jiang, L., Hsu, A., Chu, D. & Chen, R. Oxygen reduction on carbon supported Pt and PtRu catalysts in alkaline solutions. *J. Electroanal. Chem.* **629**, 87–93 (2009).
40. Guo, Z. *et al.* Self-assembled hierarchical micro/nano-structured PEDOT as an efficient oxygen reduction catalyst over a wide pH range. *J. Mater. Chem.* **22**, 17153–17158 (2012).
41. Sun, L. *et al.* Nitrogen-Doped Porous Graphitic Carbon as an Excellent Electrode Material for Advanced Supercapacitors. *Chem. Eur. J.* **20**, 564–574 (2014).

Acknowledgements

The work is supported by the National Natural Science Foundation of China (51473008, 51672019), the National Key Research and Development Program of China (2017YFA0206900).

Author Contributions

Zhichao Lin and Prof. Xiuwen Qiao designed the research work. The schematic drawing, material synthesized characterized, electrochemical measurements and analyses carried out by Zhichao Lin, Prof. Xiuwen Qiao supervised the project, with inputs from all authors.

Additional Information

Supplementary information accompanies this paper at <https://doi.org/10.1038/s41598-018-19347-5>.

Competing Interests: The authors declare that they have no competing interests.

Publisher's note: Springer Nature remains neutral with regard to jurisdictional claims in published maps and institutional affiliations.



Open Access This article is licensed under a Creative Commons Attribution 4.0 International License, which permits use, sharing, adaptation, distribution and reproduction in any medium or format, as long as you give appropriate credit to the original author(s) and the source, provide a link to the Creative Commons license, and indicate if changes were made. The images or other third party material in this article are included in the article's Creative Commons license, unless indicated otherwise in a credit line to the material. If material is not included in the article's Creative Commons license and your intended use is not permitted by statutory regulation or exceeds the permitted use, you will need to obtain permission directly from the copyright holder. To view a copy of this license, visit <http://creativecommons.org/licenses/by/4.0/>.

© The Author(s) 2018